Nano Energy 67 (2020) 104224

Contents lists available at ScienceDirect

Nano Energy

journal homepage: http://www.elsevier.com/locate/nanoen

Full paper

Iodine-assisted antisolvent engineering for stable perovskite solar cells with efficiency >21.3 %

Fengyou Wang [a,b,c], Meifang Yang [a,b,c], Shuo Yang [e], Xin Qu [a,b,c], Lili Yang [a,b,c,*], Lin Fan [a,b,c], Jinghai Yang [a,b,c,f,**], Federico Rosei [a,d]

[a] Key Laboratory of Functional Materials Physics and Chemistry of the Ministry of Education, Jilin Normal University, Changchun, 130103, China
[b] National Demonstration Center for Experimental Physics Education, Jilin Normal University, Siping, 136000, China
[c] Key Laboratory of Preparation and Application of Environmental Friendly Materials, Ministry of Education, Jilin Normal University, Changchun, 130103, China
[d] Center for Energy, Materials and Telecommunications, Institut National de La Recherche Scientifique, 1650 Boulevard Lionel-Boulet, Varennes, J3X 1S2, Québec, Canada
[e] Changchun Institute of Optics, Fine Mechanics and Physics, Chinese Academy of Sciences, Changchun, 130033, China
[f] Si Ping Hong Zui University Science Park, Siping, 136000, China

ARTICLE INFO

Keywords:
Antisolvent engineering
Perovskite solar cells
Defect passivation
Crystallization
Power conversion efficiency

ABSTRACT

The quality of the photoactive film is a significant factor in determining the power conversion efficiency (*PCE*) and the stability of perovskite solar cells (PSCs). We report a simple upgraded antisolvent washing treatment using iodine modulation, which significantly improves the $MAPbI_3$ films with high crystallinity and chemical uniformity. A detailed model for improving the mechanism is proposed to describe how the upgraded antisolvent enhances both the perovskite crystallization and passivates the under-coordinated Pb^{2+} dangling bond. PSCs fabricated with the FTO/TiO_2/$MAPbI_3$/Spiro-OMeTAD/Ag architecture used high quality films with less defective surfaces, present a *PCE* of 21.33%, retaining 91% of its initial value in ambient without any encapsulation after 30 days. These results provide insight into the surface defect passivation process achieved by halide ions balance while providing a simple and efficient process that can be extensively used to fabricate high-quality perovskite films.

1. Introduction

Perovskite solar cells (PSCs) have been widely studied for their excellent photoelectric properties and high power conversion efficiency (*PCE*) and low-cost for large-scale production. Less than ten years since the first report, the current record value of *PCE* exceeds 23% [1–4], demonstrating their promising suitability for future photovoltaic technologies. Besides harvesting solar radiation, the perovskite-based photoactive layer plays a crucial role in determining device performance, as it simultaneously exhibits ambipolar charge transport, which facilitating the collection of photogenerated charge carriers [5]. However, the inability to exactly control the crystallization process typically lead to limited control of the perovskite films morphology, grain boundaries and trap states, resulting in lower device performance [6,7]. Major works have focused on addressing the aforementioned issues, leading to encouraging progress. This includes operating solution casting conditions such as solvent engineering [8], vapor-assisted solution deposition [9], hot-substrate casting [10], some post-treatments, including antisolvent rinses [8,11,12], and solvent annealing of as-cast films [13,14]. Among these methods, antisolvent washing is a widely used in the production of dense and uniform solution-processed perovskite films because of its efficiency and simplicity [15]. Jeon et al. [16] reported that add antisolvent to freeze the precursor component immediately after spinning by rapidly removing surfeit solvent and quickly forming an intermediate phase (MAI-PbI_2-DMSO), yielding a uniformly transparent thin layer. Although antisolvent washing is almost essential in the manufacture of smooth and dense perovskite films, it is known to cause defects, especially on the film's surface. As shown by Mathews et al.

* Corresponding author. Key Laboratory of Functional Materials Physics and Chemistry of the Ministry of Education, Jilin Normal University, Changchun, 130103, China.
** Corresponding author. Key Laboratory of Functional Materials Physics and Chemistry of the Ministry of Education, Jilin Normal University, Changchun, 130103, China.
E-mail addresses: llyang1980@126.com (L. Yang), jhyang1@jlnu.edu.cn (J. Yang).

https://doi.org/10.1016/j.nanoen.2019.104224
Received 26 May 2019; Received in revised form 16 October 2019; Accepted 21 October 2019
Available online 24 October 2019

[17], antisolvent washing increased the density of defect state due to the formation of MA^+ vacancies in the perovskite thin film. Mhaisalkar et al. [18] showed that constituents such as low boiling points MAI excess and residual solvent during annealing easily evaporate from the perovskite film, leading to a significant large number of defects, specifically on the surface of the film. Since these defects (especially surface defects) are related to poor morphology and crystallization, typically act as charge traps and non-radiative recombination centers, which are used to limiting the short-circuit current density (J_{sc}) and open-circuit voltage (V_{oc}), to reduce the fill factor (*FF*), and even hysteresis effects, these are issues to be addressed to obtain the PSCs with high performance [18–21].

Lately, many improved antisolvent washing treatments have been shown to favorably reduce the surface defects in perovskite films, such as conjugated polymer-doping and solvent-engineering [16,22–25]. For instance, Zhang et al. [22] and Grätzel et al. [23] revealed an effective technique for controlling the nucleation and crystal growth of perovskite films by adding compounds like [6,6]-phenyl-C61-butyric acid methyl ester and poly (methyl methacrylate) in the antisolvent. This approach was found to enhance the efficiency and stability of the PSCs synchronously. However, the formation of PbI_2 in the perovskite film is unavoidable because the MAI is decomposed into MA^+ in the precursor solution, even before the onset of the film growth [26]. Thus, introduction of an iodine ion (I^-) additives into the precursor solution can recover methylamine into MAI to effectively passivate the defects and increase the composition of PbI_6^{4-}, therefrom outstandingly inhibiting the decomposition of $MAPbI_3$ perovskite film [27,28]. This concept defines a special opportunity for defect passivation based on coordination chemistry.

Here, we successfully introduced a facile method to achieve a high quality $MAPbI_3$ perovskite films consisting of increased particle size and reduced trap density via an iodine-assisted antisolvent engineering. When dripping the iodine-assisted antisolvent on the precursor films, the I^- within the antisolvent soaks the precursor films and then passivates the Pb^{2+} dangling bonds by forming high coordination of iodoplumbate complexes $PbI_x^{(x-2)-}$ (x = 3,4,5) in the precursor [29]. In addition, the interactions between I^- and precursors during solution casting enhance the heterogeneous nucleation of the crystalline solvate, facilitating the formation of dense films with large particle size. PSCs fabricated using this method with an FTO/TiO_2/$MAPbI_3$/Spiro-OMeTAD/Ag device architecture exhibit enhanced output performances and significantly improved stability at ~45% humidity.

2. Experimental section

Fabrication of PSCs: FTO glass substrates were sonicated for 20 min with deionized water, ethyl alcohol, acetone, and ethyl alcohol then washed under UV-ozone for 20 min. The compact TiO_2 was deposited on the FTO-coated glass by spin coating the solution at 2000 revolutions per minute (RPM) for 30 s and then annealed at 135 °C for 10 min. The mesoporous TiO_2 colloid was diluted with ethyl alcohol at a weight ratio of 1:7, and then spin-coated on the compact TiO_2 film to prepare a mesoporous TiO_2 substrate. The latter layers were first dried at 135 °C for 10 min and then sintered at 500 °C for 30 min in ambient atmosphere. Subsequently 462 mg of PbI_2 and 163 mg of MAI were dissolved in a mixed solvent of Dimethyl sulfoxide (DMSO) and Dimethylformamide (DMF) (v: v = 3:7) and stirred. The iodine (I_2) in the upgraded antisolvent was ball milled at low temperature before mixing. The precursor solution was spin coated onto the mesoporous TiO_2 layer at 4000 rpm, and an antisolvent solution with different concentrations of I_2/CB was dripped at the tenth second. Then, the obtained precursor film was annealed at 60 °C for 5 min and 100 °C for 10 min to grow the perovskite film. The entire perovskite film is manufactured in a nitrogen glove box. Hole transport layers were then prepared by mixing 72.3 mg of Spiro-OMeTAD, 28.5 μL with a solution of 500 mg mL^{-1} Li-TFSI in acetonitrile and 18.5 μL of 4-*tert*-butylpyridine in 1 mL of chlorobenzene. The 80 μL of the mixture solution was spin-coated on the prepared $MAPbI_3$ films at 3000 RPM for 30 s. Finally, the silver counter electrode was vacuum evaporated at the top.

More details about the corresponding materials and characterization were provided in the supporting information as Supplementary Notes 1 and 2, respectively.

3. Results and discussion

Initially, to examine the quality of the perovskite absorber layer, we used a scanning electron microscopy (SEM) image the film morphology to identify the shape and measure the coverage of the $MAPbI_3$ grains and thin films. Different weights of I_2 were dissolved in CB to obtain a mixed solution (0, 0.01, 0.05 and 0.12 mg mL^{-1}) as an antisolvent for the $MAPbI_3$ film. For simplicity, the corresponding samples of different concentrations of I_2/CB mixed antisolvent were named Control, M − 1, M − 5 and M − 12, respectively. Fig. 1a–d displays top-view SEM images of the perovskite films prepared using various antisolvents. And Fig. S1 clearly compares the statistical particle size distribution made according to Fig. 1a–d. A typical pinhole-free perovskite film with a particle size of ~260 nm was obtained by using pure CB as antisolvent (Fig. 1a). When increasing the concentration of I_2 to M − 5, the particle size grows up to ~450 nm and the grain boundary density is reduced. As shown in the atomic force microscopy (AFM) images of Fig. 1e–g, the roughness is also reduced from 23.7 nm of the control sample to 11.2 nm of the M − 5 sample. Large grains with low grain boundary density result in a lower defect density and charge leakage between the hole transport layers and the electron transport layers. However, further increasing the I_2 concentration to M − 12 is detrimental to the crystallization of the perovskite films. During the following heating treatment, the excess I_2 in the precursor films will be precipitated or forms deep level defects such as interstitial iodine, thereby affecting the defect density and the stability of the device [30,31]. We speculate that the residual I_2 may act as a nonradiative recombination center [32] in the perovskite films during the annealing treatment, which induces pinholes and increases the roughness of the perovskite surface to 25.8 nm (Fig. 1h and i). In order to indicate the effect of upgraded antisolvent on the morphology of the perovskite films, we first researched the effect of changing the composition of the antisolvent. The absorption spectra of the upgraded antisolvent with different levels of I_2 concentration are shown in Fig. 1j. We found that the absorbance peak at 500 nm increases with rising I_2 concentration. As reported by Benesi et al. this peak is not attributed to halogens nor CB, but only to the charge transfer complex $I_2{\cdot}C_6H_5Cl$ (inset of Fig. 1j) [33]. Moreover, when dripping DMSO/DMF into the upgraded antisolvent, the absorbance peak at 500 nm dramatically decreased, while a characteristic peak at 350 nm appeared (Fig. 1k). The absorbance peak at 350 nm is attributed to the presence of I_3^- in the solution (Fig. S2), which means that the $I_2{\cdot}C_6H_5Cl$ in the upgraded antisolvent can be further decomposed into CB and I_3^- by DMSO/DMF [34–36]. Therefore, in the growth of the perovskite films, when the upgraded antisolvent was dripped onto the precursor surface, the DMSO/DMF in the perovskite precursor first decomposed $I_2{\cdot}C_6H_5Cl$ to CB and I_3^-.

With this information at hand, we monitored the intermediate-phase conversion of the control and M − 5 samples by acquiring *in situ* XRD patterns under variable temperature. As shown in Fig. 2a, the pre-perovskite intermediates (MAI-PbI_2-DMSO) can be observed at room temperature by XRD peaks at low angles (6.55°, 7.21° and 9.17°) [20]. When the solvent is extracted from the intermediate solvate, the MAI-PbI_2-DMSO complexes provide a template that serves as framework for further growth of $MAPbI_3$ [23]. We found that the XRD intensity of the M − 5 sample is higher than the control sample at room temperature, which implies that the negative I_3^- in M − 5 triggers heterogeneous nucleation of the perovskite precursor [22,23]. When the temperature was raised to 60 °C, the low-angle diffraction peak related to the pre-perovskite intermediates disappears and the diffraction peak of the

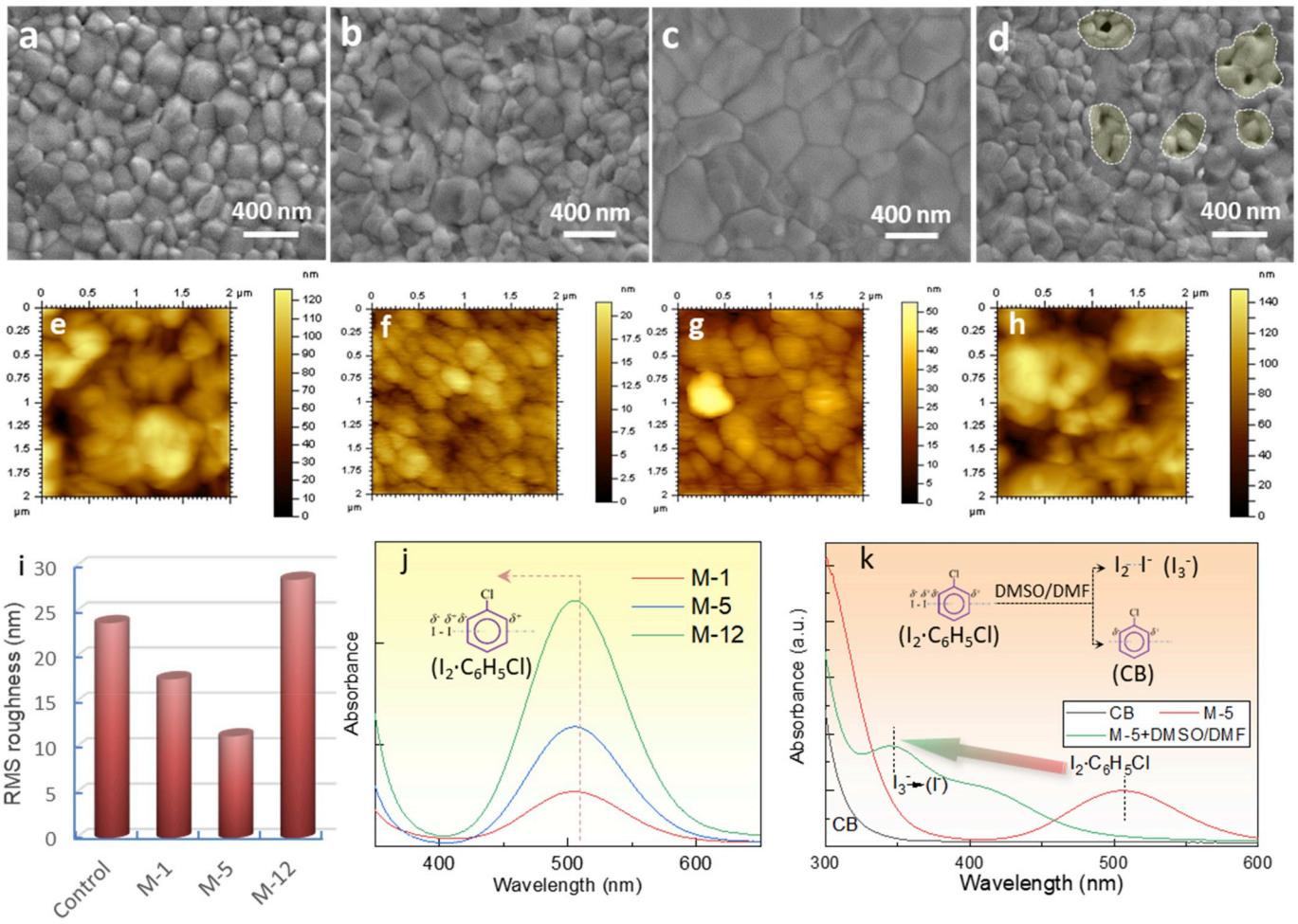

Fig. 1. Analysis of the crystallization enhancement induced by upgraded antisolvent. SEM images of perovskite films fabricated from (a) control, (b) M – 1, (c) M – 5, and (d) M – 12 antisolvent, respectively. The dash circles highlight the pinholes in the perovskite films. AFM images of perovskite films fabricated from (e) control, (f) M – 1, (g) M – 5, and (h) M – 12 antisolvent, respectively. (i) The corresponding RMS roughness of the samples. (j) The absorbance of the different antisolvent. Inset: scheme of the atomic structure for charge transfer complex $I_2{\cdot}C_6H_5Cl$. (k) The absorbance of CB, M – 5, and M-5+DMSO/DMF solution. Inset: scheme of $I_2{\cdot}C_6H_5Cl$ decomposition.

$MAPbI_3$ perovskite appears (~14°). The diffraction intensity of the control sample was higher than the case of the M – 5 sample in this initial stage, demonstrating that the crystallization of the latter is delayed. After heating at 100 °C for 10 min, all solvents evaporated from the precursors (Fig. S3). The XRD peak intensity of the M – 5 sample becomes much higher than the control sample (the detailed comparison is shown in Fig. S4), which indicates improved crystallization. The above results indicate that the M – 5 antisolvent could accelerate nucleation and delay crystallization in the perovskite film growth. The slower crystallization may result from the $I_2{\cdot}C_6H_5Cl$ in the antisolvent extending the solvent extraction process. As reported by Grätzel et al. fast nucleation could temperate crystal growth and the delayed crystallization could minimize the total Gibbs free energy, thus making the crystals grow in the thermodynamically preferred orientation [23]. In this case, iodine-assisted antisolvent engineering allows both of these objectives to be achieved simultaneously, and the cooperation of these two effects results in smooth perovskite films with larger grains.

Except for the improved crystallization, Pb^{2+} is coordinated to six I^- ligands in both the PbI_2 rhombus structure and the methylammonium lead iodide structure. Depending on the coordination chemistry, various iodoplumbate coordination complexes such as PbI_3^-, PbI_4^{2-}, PbI_5^{3-}, and PbI_6^{4-} may be present in the precursor solution, but in addition to the highly coordinated PbI_6^{4-} favored to formation defect-free perovskite films, great majority of the iodoplumbate coordination complexes may result in the perovskite structural defects [20]. Here, we performed numerical simulation by density functional theory to analyze the trap states evaluation in the $MAPbI_3$ films with different iodine vacancies (I_v). Fig. 3 shows the density of states and model electron density of the $MAPbI_3$ films with 0-, 1-, and 2- I_v. Apparently, for the $MAPbI_3$ films with I_v, there is a trap level within the bandgap which is mainly ascribed to Pb orbits, due to the fact that the localized charge distribution of the low coordinated Pb. The depth and the intensity of the trap states increase as the I_v increases. On the other hand, this also indicates the defect level can be eliminated when gradually delocalized the charge distribution by passivating the Pb dangling bonds.

The uncoordinated I^- has four lone electron pairs which enable it to be shared simultaneously with multiple Pb^{2+} ion. In the iodine-assisted antisolvent engineering, the induced I^- will penetrate into the MAI-PbI_2-DMSO colloids during solvent extraction, and coordinate with Pb^{2+} to form a highly coordinated lead acid species (Fig. 4a) and terminate the Pb^{2+} dangling bonds at grain boundaries. To further interpret this mechanism, we examined the evolution of iodoplumbate coordination complexes as a function of increasing I_2 concentration. When elevating the I_2 concentration from 0 to 0.05 mg mL^{-1} (Fig. 4b–e), different iodide-coordinated plumbate ions were obviously observed, and their absorption peaks were consistent with previous reports [37]. We found that the high I_2 concentration will trim high-coordinated lead acid species from PbI_3^- to PbI_5^{3-}, which indicates that I^- work with the lead

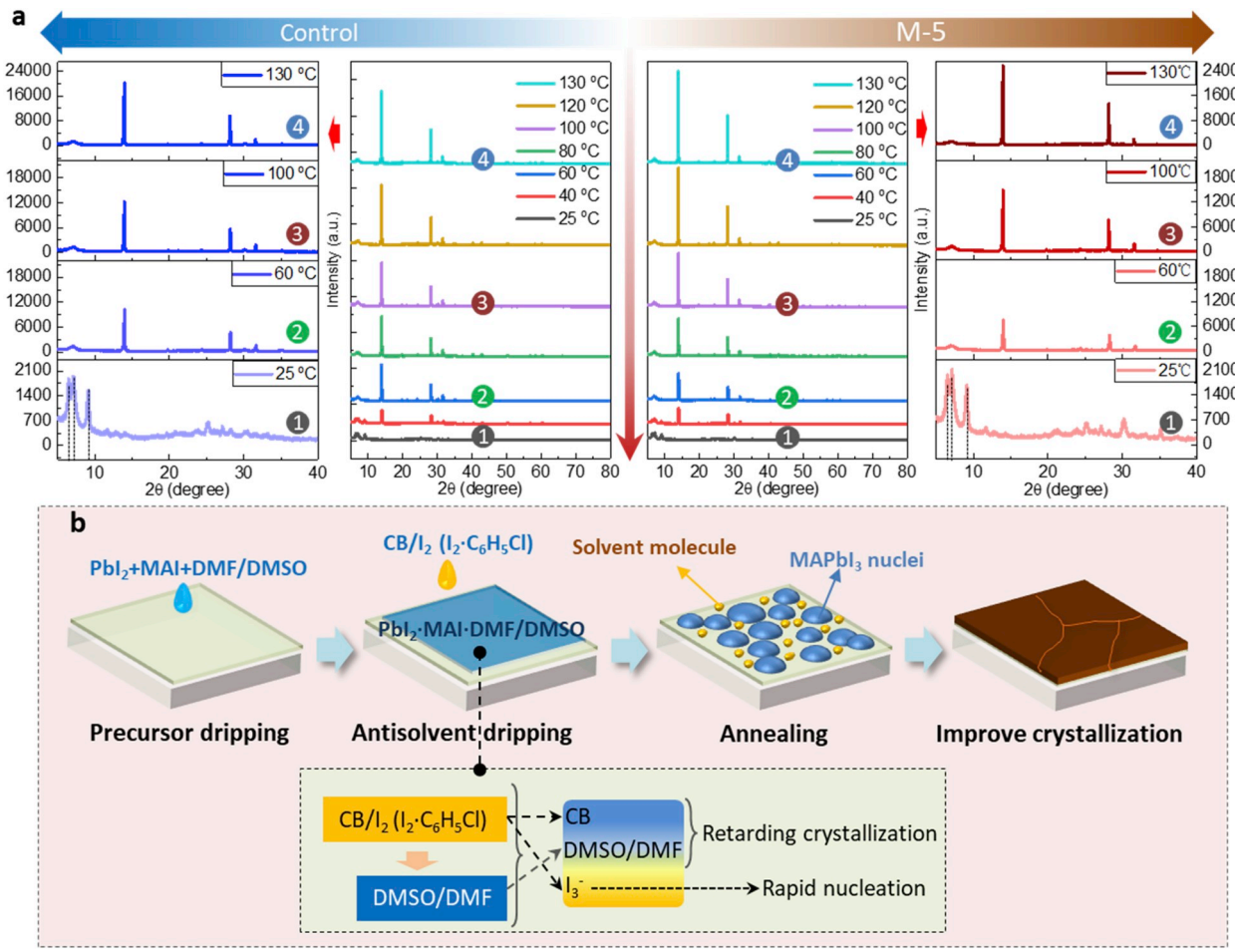

Fig. 2. (a) *In situ* XRD patterns of the control (left) and M – 5 (right) samples as a function of increasing temperature. We chose four typical temperatures (1, 2, 3, and 4) to finely compare the detailed evolution of crystallization. (b) Schematic diagram of the antisolvent process.

acid species to form a high-coordination state. In addition, we performed FTIR tests on precursor solutions with and without I_2·CB, further demonstrating that I^- work with the lead acid species to form a high-coordination state. As shown in Fig. S5, in the precursor solution without I_2·CB, the stretching vibration of C═O is at 1646 cm^{-1} due to the weak C═O bond strength interaction with PbI_2. After the addition of I_2·CB to the precursor solution, the stretching vibration was red-shifted to 1665 cm^{-1} due to the strong coordination of I^- and $PbI_x^{(x-2)-}$. This also indicates that the I^- ions coordinate with the Lewis acid $PbI_x^{(x-2)-}$ and thereby passivate the traps at the grain boundaries or at perovskite surface.

We then performed a systematic characterization to study the defects in the control and M – 5 samples. Steady-state photoluminescence (PL) spectroscopy is a valid technique for detecting trap states in the perovskite films. Here, the signal responses based on the glass/perovskite structure were recorded (Fig. 5a). We found a significant increase in PL intensity by M – 5 antisolvent washing, which is attributed to a reduction of the non-radiative recombination by passivated deep-level energy defects. In addition, a slight blue shift of the PL peak was observed for the M – 5 sample, indicating that the spontaneous radiative recombination between band tail states is reduced (as illustrated in Fig. S6) [38]. Time-resolved photoluminescence (TRPL) spectroscopy was performed to further investigate carrier recombination (Fig. 5b). By fitting the TRPL, the control sample exhibits an average carrier lifetime of 313.48 ns, while in the M – 5 the average lifetime increases to 687.38 ns. The trap density variations of the devices were also studied from dark *J-V* curves of the electron-only devices FTO/TiO_2/$MAPbI_3$/PCBM/Ag. Fig. 5c and d shows the dark *J-V* curves, which is quantitatively measured by the trap-filling limit voltage (V_{TFL}) obtained by space charge limited current (SCLC) [32]. The trap density can be determined from V_{TFL} by referring to the relationship $V_{TFL} = eN_tL^2/2\varepsilon\varepsilon_0$, where the relative dielectric constant ε of $MAPbI_3$ is 32, the vacuum dielectric constant ε_0 is 8.854×10^{-12} F m^{-1}, and L is the thickness of the perovskite film of 350 nm [39,40]. We estimated the calculated trap density (N_t) to be 5.6×10^{15} cm^{-3} and 8.35×10^{16} cm^{-3} for the M – 5 sample and the control sample, respectively. We further examined the Urbach energy (E_u) of the films, which provide important information about the disorder of shallow energy levels by detecting the sharp onset of absorption (Fig. S7) at the direct bandgap [41]. We found that the E_u value of the M – 5 sample was reduced (Fig. 5e). The smaller E_u value obtained in the M – 5 sample is consistent with the longer non-radiative recombination lifetime and blue-shift as observed in TRPL and PL measurements, indicating a lower trap density.

We then examined the photovoltaic performance of the PSCs with traditional antisolvent (CB) and iodine-assisted antisolvent treatment, respectively. Fig. 6a shows the scheme and cross sectional SEM images of the PSC device fabricated using the FTO/TiO_2/perovskite/spiro-OMeTAD/Ag architecture. The *J-V* characteristics (under AM 1.5 G illumination with light intensity of 100 mW cm^{-2}) of the control and M – 5 PSCs are shown in Fig. 6b. The control device exhibits a hysteresis of 0.89% (*reverse scan*: V_{oc} ~1.11 V, J_{sc} ~21.32 mA cm^{-2}, *FF* ~77.1%, *PCE* ~18.22%; *forward scan*: V_{oc} ~1.11 V, J_{sc} ~20.49 mA cm^{-2}, *FF* ~76.2%, *PCE* ~17.33%). In contrast, M – 5 devices have shown significant improvements in V_{oc}, J_{sc}, and *FF*. M – 5 solar cells presented the best performance with lower value of hysteresis of 0.44% (*reverse scan*: V_{oc} ~1.17 V, J_{sc} ~22.77 mA cm^{-2}, *FF* ~80.1%, *PCE* ~21.33%; *forward*

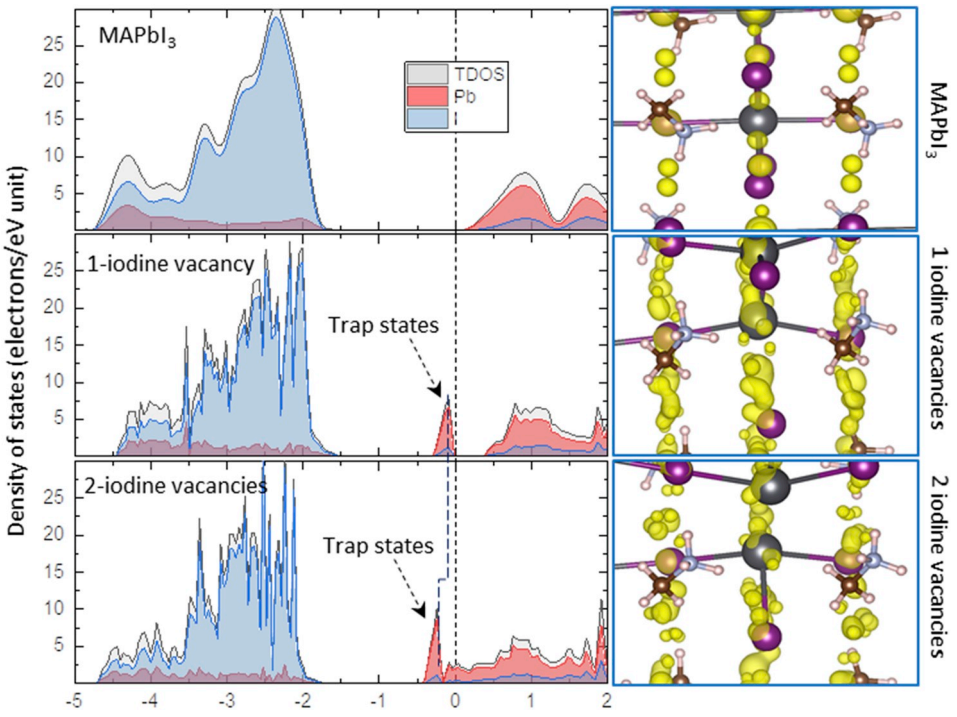

Fig. 3. The density of states (left) and the model electron density (right) of the $MAPbI_3$ with 0-, 1- and 2 I_v. The Fermi level is set to zero. The total density of states, Pb, and I are assigned as gray, pink, and blue. The depth and intensity of the trap states increases as the I_v increase.

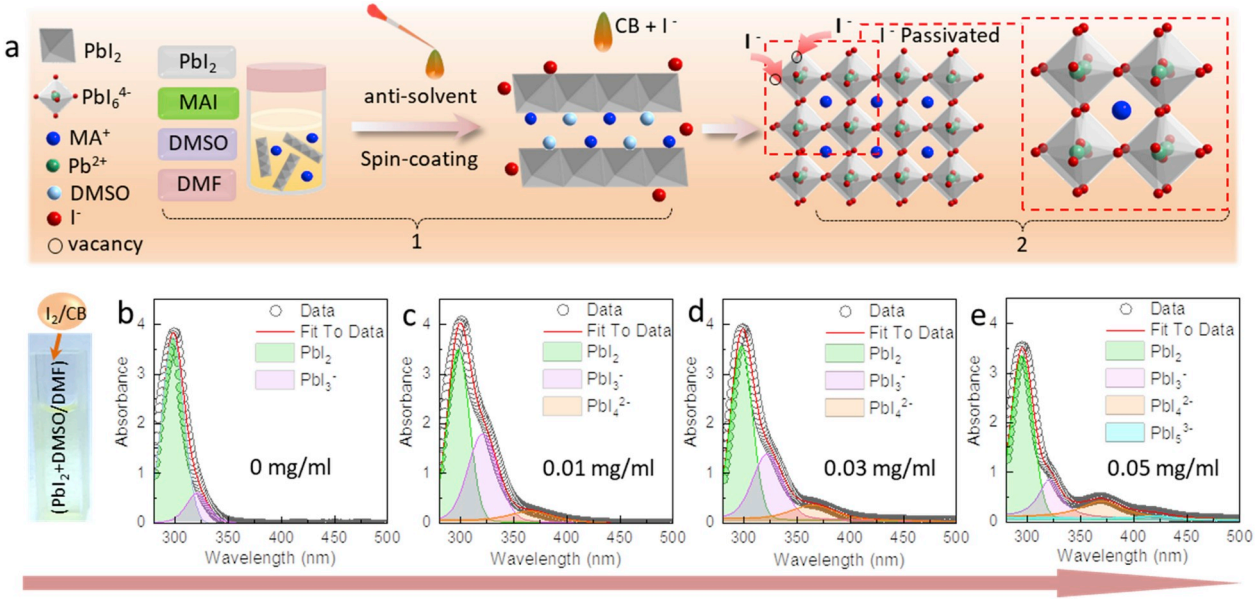

Fig. 4. Passivation mechanism of the upgraded antisolvent. (a) The schematic of grain growth mechanism: Process (1), dissolution, mixing, and dripping process (PbI_2, MAI, DMF, and DMSO fully dissolve and mix under continuous stirring); Process (2), interaction and grains growth process. The I^- decomposed from I_3^- could be the ligands coordinating to Pb^{2+} defects. (b–e) The change in the UV absorption spectra of PbI_2 in DMF/DMSO as the concentration of I_2 increased. Overlaid on the spectra are example fit functions for the main complexes (including: PbI_2, PbI_3^-, PbI_4^{2-}, and PbI_5^{3-}).

scan: V_{oc} ~1.17 V, J_{sc} ~22.39 mA cm^{-2}, *FF* ~79.7%, *PCE* ~20.89%). We also analyzed the distributions of *PCEs* based on 20 individual devices for both control and M – 5 samples. A detailed parameter comparison of 20 perovskite solar cells (10 control cells and 10 M – 5 cells) is shown in Fig. S8. The output parameters distribution of M – 5 cells is denser than the control ones, which means that the M – 5 cells have better reproducibility. This can be expected from the sufficient passivation capability of the upgraded antisolvent engineering approach, which passivates the defects induced by manufacturing process and then eliminates the performance fluctuating. The stabilized *PCE* of the control and M – 5 cells were measured. The real power output of the device was extracted by monitoring the photocurrent under the bias of the maximum power point under AM 1.5G illumination. The M – 5 cell exhibited a stabilized efficiency of 20.05% at the maximum power point (0.995 V) for testing over 100 s, while the control cell showed only 17.43% stability at the maximum power point (0.943 V) (Fig. S9). The plot of the external quantum efficiency (EQE) as a function of wavelength of the PSCs is shown in Fig. 6c. As expected, the spectral response

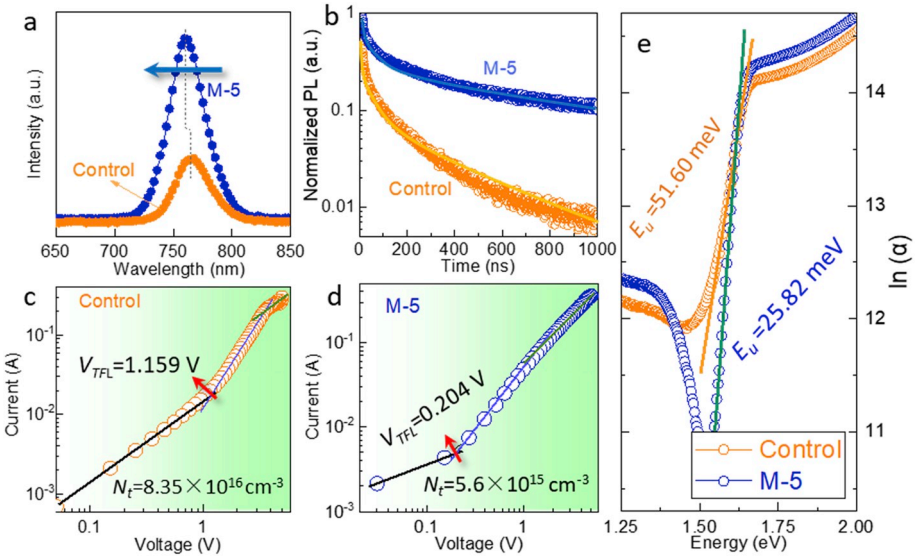

Fig. 5. Study on the defects of the perovskite films based on traditional/upgraded antisolvent strategies. The (a) PL spectra and (b) TRPL for the control and M – 5 samples, respectively. A blue shift can be observed for the PL spectra. (c–d) The SCLC curves of the control and M – 5 samples, respectively. The architecture for measurement is FTO/TiO_2/$MAPbI_3$/PCBM/Ag and (e) E_u values for the control and M – 5 samples, respectively.

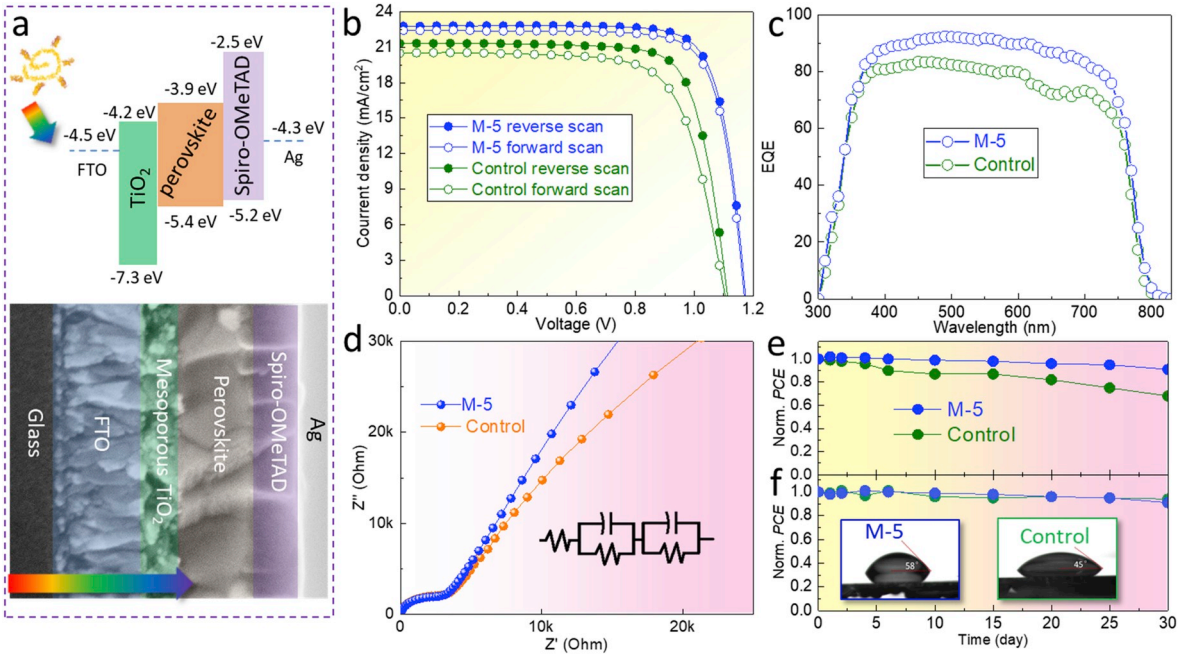

Fig. 6. Device performance. (a) The schematic architecture and the cross-section of the PSCs. (b) The illuminated *J-V* curves of the solar cells under reverse- and forward-scan, respectively. (c) The EQE and (d) Nyquist plot of PSCs. The inset of d shows the equivalent circuit used for fitting the plots. The stability of corresponding devices (e) in ambient environment and (f) in nitrogen atmosphere, respectively. Inset: The contact angle of the M – 5 and control perovskite films.

of the M – 5 device in the 350–800 nm wavelength range is superior to that of the control device. All these results demonstrate that the iodine-assisted antisolvent engineering plays a key role in improving the quality of perovskite films with fewer grain boundaries and large grains, which enhances V_{oc}, *FF* and spectral response.

Electrochemical impedance spectroscopy (EIS) was used to further characterize the charge carrier transport and recombination properties of our PSC. The Nyquist plot of the device with the frequency range of 100 Hz to 1 MHz measured in the dark is shown in Fig. 6d. The Nyquist plots were fitted using an equivalent circuit model (inset in Fig. 6d) with two semicircles corresponding to high frequency transfer resistance (R_{tr}) and low frequency recombination resistance (R_{rec}) [42–47]. The value of R_{tr} shows little variation for these two devices, indicating no significant effect on the charge transfer properties. The second arc is attributed to the recombination resistance (R_{rec}) [48–50]. The R_{tr} of both control and M – 5 cells are almost the same, indicating that the charge transfer at the hetero-interface is unlikely to be the cause of the performance differences. However, the curve of R_{rec} for the M – 5 sample has a larger value than the control sample, indicating that the M – 5 doped sample has smaller recombination. As mentioned above, compared with the traditional antisolvent strategy (control), better crystallization and lower defect density were achieved by using the upgraded technique (M – 5) for perovskite films, thereby reducing charge losses within the device.

In addition to increasing the *PCE*, a major challenge in deploying

PSCs as a commercial technology consists in improving stability. Besides increasing photovoltaic efficiency, high quality films also enhance stability. We examined the stability of the PSCs over a period of 30 days under ambient conditions (Fig. 6e, ~45% humidity) and nitrogen atmosphere (Fig. 6f), respectively. In nitrogen atmosphere, both M – 5 and control cells exhibit good stability (i.e. retaining >93% of the initial *PCE*) after 30-days measurement (under periodic illumination). A slight reduction in *PCE* for both PSCs may result from repeated testing, which may damage the electrode after repeated testing. However, in ambient conditions, M – 5 devices show much higher stability (~91% of the initial *PCE*) than the control cells (retaining ~70% of the initial *PCE*). We stored the control and M – 5 perovskite films in ambient conditions for 25 days (~30% humidity, in dark), then characterized them using XRD. No PbI_2 peaks were observed before storing the samples. However, after 25 days, the XRD pattern showed a new diffraction peak attributed to PbI_2 at 12.8° for the control perovskite film, which may result from the decomposition of $MAPbI_3$ [37]. In contrast, still no PbI_2 peaks are observed for the M – 5 film (Fig. S10). The enhanced stability of the $MAPbI_3$ films is ascribed to the dense morphology and fewer defects that inhibit MA^+ motion and desorption from grain boundaries. We also found that iodine-assisted antisolvent engineering yields a surface with superior hydrophobicity, which was further confirmed by the water contact angle measurement (inset of Fig. 6f). The derived contact angles are 45° and 58° for the control and M – 5 perovskite films, respectively. The increase in contact angle demonstrates a strongly hydrophobic of the perovskite layer that provides a theoretical basis for its enhanced stability in a humid environment.

4. Conclusions

In short, we developed an I_2 modulated antisolvent strategy, which allows fabricating highly crystallized defect-less $MAPbI_3$ perovskite films with high stability. The interactions between I^- and precursors triggers the enhanced heterogeneous nucleation of the crystalline solvate during solution casting, which facilitates the growth of dense films. Simultaneously, the I^- make the Pb-I complexes to a high-coordinated lead acid species and terminate under-coordinated Pb^{2+} dangling bonds, yielding better passivation due to lower trap states. A *PCE* of 21.33% was achieved with 0.44% hysteresis for the M – 5 samples, while for the control one, the hysteresis is 0.89%. The *PCE* of the M – 5 sample is ~15.9% higher than the *PCE* of 18.22% obtained for the control PSC. Concerning the stability, a slight degradation of only ~9% was measured after 30 days of exposure to ~45% relative humidity at room temperature, without encapsulation. The enhanced performance and improved moisture stability of the M – 5 device compared to the control PSC can be primarily attributed to improved crystallization, fewer defects, and superior hydrophobicity. Our work therefore demonstrates that defect passivation of perovskite films using halogen-doped antisolvent processing is a practical and effective method towards defect-free $MAPbI_3$ films for environmentally stable high performance PSCs.

Declaration of competing interest

We declare that we have no financial, commercial, and personal relationships with other people or organizations that can inappropriately influence our work, there is no professional or other personal interest of any nature or kind in any product, service and/or company that could be construed as influencing the position presented in, or the review of, the manuscript entitled.

Acknowledgements

The authors gratefully acknowledge the support from the National Natural Science Foundation of China (Grant Nos. 11904127, 61904066, and 61775081), Program for the development of Science and Technology of Jilin province (Item No. 20180520182JH, 20180519016JH), and the Thirteenth Five-Year Program for Science and Technology of Education Department of Jilin Province (Item No. JJKH20180759KJ, JJKH20190998KJ), Talent Development Fund Project in Jilin Province, Special Project of Industrial Technology Research and Development in Jilin Province (2019C042-2). Construction Program for Innovation Research Team of Jilin Normal University (Grant No.201703). F.R. is grateful to the Canada Research Chairs program for partial salary support.

Appendix A. Supplementary data

Supplementary data to this article can be found online at https://doi.org/10.1016/j.nanoen.2019.104224.

References

[1] F. Wang, Y. Zhang, M. Yang, L. Fan, L. Yang, Y. Sui, J. Yang, X. Zhang, Nano Energy 60 (2019) 198.
[2] C. Aranda, A. Guerrero, J. Bisquert, ACS Energy Lett. 4 (2019) 741.
[3] J. Emara, T. Schnier, N. Pourdavoud, T. Riedl, K. Meerholz, S. Olthof, Adv. Mater. 28 (2016) 553.
[4] H. Hu, F. Meier, D. Zhao, Y. Abe, Y. Gao, B. Chen, T. Salim, E.E.M. Chia, X. Qiao, C. Deibel, Y.M. Lam, Adv. Mater. 30 (2018) 1707621.
[5] F. Liu, Q. Dong, M.K. Wong, A.B. Djurišić, A. Ng, Z. Ren, Q. Shen, C. Surya, W. K. Chan, J. Wang, A.M.C. Ng, C. Liao, H. Li, K. Shih, C. Wei, H. Su, J. Dai, Adv. Energy Mater. 6 (2016) 1502206.
[6] C. Chen, Z. Song, C. Xiao, D. Zhao, N. Shrestha, C. Li, G. Yang, F. Yao, X. Zheng, R. J. Ellingson, C.-S. Jiang, M. Al-Jassim, K. Zhu, G. Fang, Y. Yan, Nano Energy 61 (2019) 141–147.
[7] X. Gong, Z. Huang, R. Sabatini, C.-S. Tan, G. Bappi, G. Walters, A. Proppe, M. I. Saidaminov, O. Voznyy, S.O. Kelley, E.H. Sargent, Nat. Commun. 10 (2019) 1591.
[8] T. Niu, J. Lu, R. Munir, J. Li, D. Barrit, X. Zhang, H. Hu, Z. Yang, A. Amassian, K. Zhao, S. Liu, Adv. Mater. 30 (2018) 1706576.
[9] Q. Chen, H. Zhou, Z. Hong, S. Luo, H. Duan, H. Wang, Y. Liu, G. Li, Y. Yang, J. Am. Chem. Soc. 136 (2014) 622.
[10] Y. Deng, E. Peng, Y. Shao, Z. Xiao, Q. Dong, J. Huang, Energy Environ. Sci. 8 (2015) 1544.
[11] D. Gedamu, I.M. Asuo, D. Benetti, M. Basti, I. Ka, S.G. Cloutier, F. Rosei, R. Nechache, Sci. Rep. 8 (2018) 12885.
[12] T. Bu, L. Wu, X. Liu, X. Yang, P. Zhou, X. Yu, T. Qin, J. Shi, S. Wang, S. Li, Z. Ku, Y. Peng, F. Huang, Q. Meng, Y. Cheng, J. Zhong, Adv. Energy Mater. 7 (2017) 1700576.
[13] Q. Wang, Y. Shao, Q. Dong, Z. Xiao, Y. Yuan, J. Huang, Energy Environ. Sci. 7 (2014) 2359.
[14] C. Bi, Q. Wang, Y. Shao, Y. Yuan, Z. Xiao, J. Huang, Nat. Commun. 6 (2015) 7747.
[15] A. Dualeh, N. Tétreault, T. Moehl, P. Gao, M.K. Nazeeruddin, M. Grätzel, Adv. Funct. Mater. 24 (2014) 3250.
[16] N.J. Jeon, J.H. Noh, Y.C. Kim, W.S. Yang, S. Ryu, S.I. Seok, Nat. Mater. 13 (2014) 897.
[17] S.S. Lim, W.K. Chong, A. Solanki, H.A. Dewi, S. Mhaisalkar, N. Mathews, T.C. Sum, Phys. Chem. Chem. Phys. 18 (2016) 27119.
[18] G. Han, T.M. Koh, S.S. Lim, T.W. Goh, X. Guo, S.W. Leow, R. Begum, T.C. Sum, N. Mathews, S. Mhaisalkar, ACS Appl. Mater. Interfaces 9 (2017) 21292.
[19] A. Möllmann, D. Gedamu, P. Vivo, R. Frohnhoven, D. Stadler, T. Fischer, I. Ka, M. Steinhorst, R. Nechache, F. Rosei, S.G. Cloutier, T. Kirchartz, S. Mathur, Adv. Eng. Mater. 21 (2019) 1801196.
[20] Z. Liu, J. Hu, H. Jiao, L. Li, G. Zheng, Y. Chen, Y. Huang, Q. Zhang, C. Shen, Q. Chen, Adv. Mater. 29 (2017) 1606774.
[21] D. Bi, P. Gao, R. Scopelliti, E. Oveisi, J. Luo, M. Grätzel, A. Hagfeldt, M. K. Nazeeruddin, Adv. Mater. 28 (2016) 2910.
[22] F. Zhang, W. Shi, J. Luo, N. Pellet, C. Yi, X. Li, X. Zhao, T.J.S. Dennis, X. Li, S. Wang, Y. Xiao, S.M. Zakeeruddin, D. Bi, M. Grätzel, Adv. Mater. 29 (2017) 1606806.
[23] D. Bi, C. Yi, J. Luo, J.-D. Décoppet, F. Zhang, S.M. Zakeeruddin, X. Li, A. Hagfeldt, M. Grätzel, Nat. Energy 1 (2016) 16142.
[24] X. Zheng, B. Chen, C. Wu, S. Priya, Nano Energy 17 (2015) 269.
[25] Z.-K. Wang, M. Li, Y.-G. Yang, H. Hu, H. Ma, X.-Y. Gao, L.-S. Liao, Adv. Mater. 28 (2016) 6695–6703.
[26] T.J. Jacobsson, J.-P. Correa-Baena, E.H. Anaraki, B. Philippe, S.D. Stranks, M. E. Bouduban, W. Tress, K. Schenk, J. Teuscher, J.-E. Moser, H. Rensmo, A. Hagfeldt, J. Am. Chem. Soc. 138 (2016) 10331.
[27] G.J.A. Wetzelaer, M. Scheepers, A.M. Sempere, C. Momblona, J. Ávila, H.J. Bolink, Adv. Mater. 27 (2015) 1837.
[28] J.H. Heo, D.H. Song, H.J. Han, S.Y. Kim, J.H. Kim, D. Kim, H.W. Shin, T.K. Ahn, C. Wolf, T.W. Lee, Adv. Mater. 27 (2015) 3424.
[29] Z. Liu, J. Hu, H. Jiao, L. Li, G. Zheng, Y. Chen, Y. Huang, Q. Zhang, C. Shen, Q. Chen, Adv. Mater. 29 (2017) 1606774.
[30] Z. Liu, J. Hu, H. Jiao, L. Li, G. Zheng, Y. Chen, Y. Huang, Q. Zhang, C. Shen, Q. Chen, H. Zhou, Adv. Mater. 29 (2017) 1606774.

[31] Y. Chen, N. Li, L. Wang, L. Li, Z. Xu, H. Jiao, P. Liu, C. Zhu, H. Zai, M. Sun, W. Zou, S. Zhang, G. Xing, X. Liu, J. Wang, D. Li, B. Huang, Q. Chen, H. Zhou, Nat. Commun. 10 (2019) 1112.
[32] M.-H. Du, J. Phys. Chem. Lett. 6 (2015) 1461–1466.
[33] H.A. Benesi, J.H. Hildebrand, J. Am. Chem. Soc. 8 (1948) 71.
[34] W.S. Yang, B.-W. Park, E.H. Jung, N.J. Jeon, Y.C. Kim, D.U. Lee, S.S. Shin, J. Seo, E. K. Kim, J.H. Noh, S.I. Seok, Science 365 (2017) 1376–1379.
[35] J.M. Gardner, M. Abrahamsson, B.H. Farnum, G.J. Meyer, J. Am. Chem. Soc. 131 (2009) 16206–16214.
[36] A. Reynal, A. Forneli, E. Martinez-Ferrero, A. Sanchez-Diaz, A. VidalFerran, B. C. O'Regan, E. Palomares, J. Am. Chem. Soc. 130 (2008) 13558.
[37] S. Rahimnejad, A. Kovalenko, S.M. Forés, C. Aranda, A. Guerrero, ChemPhysChem 17 (2016) 2795.
[38] Y. Shao, Z. Xiao, C. Bi, Y. Yuan, J. Huang, Nat. Commun. 5 (2014) 5784.
[39] R.H. Bube, J. Appl. Phys. 33 (1962) 1733.
[40] Q. Dong, Y. Fang, Y. Shao, P. Mulligan, J. Qiu, L. Cao, J. Huang, Science 347 (2015) 967.
[41] Z. Tang, S. Tanaka, S. Ito, S. Ikeda, K. Taguchi, T. Minemoto, Nano Energy 21 (2016) 51.
[42] W.S. Yang, B.-W. Park, E.H. Jung, N.J. Jeon, Y.C. Kim, D.U. Lee, S.S. Shin, J. Seo, E. K. Kim, J.H. Noh, S.I. Seok, Science 356 (2017) 1376–1379.
[43] Y. Yang, S. Feng, M. Li, F. Li, C. Zhang, Y. Han, L. Li, J. Yuan, L. Cao, Z. Wang, B. Sun, X. Gao, Nano Energy 48 (2018) 10–19.
[44] Q. Dong, Z. Wang, K. Zhang, H. Yu, P. Huang, X. Liu, Y. Zhou, N. Chen, B. Song, Nanoscale 8 (2016) 5552.
[45] A. Dualeh, T. Moehl, N. Tétreault, J. Teuscher, P. Gao, M.K. Nazeeruddin, M. Grätzel, ACS Nano 8 (2014) 362.
[46] G. Xing, B. Wu, S. Chen, J. Chua, N. Yantara, S. Mhaisalkar, N. Mathews, T.C. Sum, Small 11 (2015) 3606–3613.
[47] X. Xu, H. Zhang, K. Cao, J. Cui, J. Lu, X. Zeng, Y. Shen, M. Wang, ChemSusChem 7 (2014) 3088–3094.
[48] J. Dong, Y. Zhao, J. Shi, H. Wei, J. Xiao, X. Xu, J. Luo, J. Xu, D. Li, Y. Luo, Q. Meng, Chem. Commun. 50 (2014) 13381–13384.
[49] Y. Zhao, K. Zhu, J. Phys. Chem. Lett. 4 (2013) 2880–2884.
[50] A.K. Chandiran, M.K. Nazeeruddin, M. Grätzel, Adv. Funct. Mater. 24 (2014) 1615–1623.